

## Nitride MXenes as sulfur hosts for thermodynamic and kinetic suppression of polysulfide shuttling: a computational study

Ke Fan<sup>a</sup>, Yiran Ying<sup>a</sup>, Xin Luo<sup>b\*</sup>, and Haitao Huang<sup>a\*</sup>

Received 00th January 20xx,  
Accepted 00th January 20xx

DOI: 10.1039/x0xx00000x

The practical applications of lithium-sulfur (Li-S) batteries are greatly hindered by the poor conductivity of sulfur, the shuttling of lithium polysulfides (LiPSs), and the sluggish kinetics in charge-discharge process. In order to solve these problems, here we propose the surface-functionalized V<sub>2</sub>N MXenes as the host materials to improve the electrochemical performance of the Li-S battery. Based on the density functional theory (DFT) calculations, we found that both the bare and functionalized V<sub>2</sub>NT<sub>2</sub> (T = O, F, OH, and S) exhibit metallicity, and three of them (V<sub>2</sub>NO<sub>2</sub>, V<sub>2</sub>NF<sub>2</sub>, and V<sub>2</sub>NS<sub>2</sub>) possess moderate LiPS adsorption strength, which thermodynamically benefits the suppression of the dissolution and shuttling of LiPSs. Besides, V<sub>2</sub>NS<sub>2</sub> shows the lowest Gibbs free energy barrier for sulfur reduction reaction (0.49 eV) during discharge, which kinetically suppresses the dissolution and shuttling of LiPSs by expediting the decomposition process from soluble LiPSs to insoluble ones. Moreover, the surface functionalized V<sub>2</sub>NT<sub>2</sub> also exhibit outstanding catalytic ability for Li<sub>2</sub>S decomposition during charge, which decrease the energy barrier from 3.64 eV (bare V<sub>2</sub>N) to 1.55 (V<sub>2</sub>NO<sub>2</sub>) and 1.19 eV (V<sub>2</sub>NS<sub>2</sub>), and increase the charging kinetics. Based on these results, V<sub>2</sub>NS<sub>2</sub> monolayers are suggested as promising host materials for S cathodes due to the fast charge/discharge kinetics and effective suppression of LiPS shuttling. This theoretical study provides further insight into the application of nitride MXenes and other two-dimensional materials as conductive anchoring materials for Li-S batteries.

### 1. Introduction

In recent years, battery technology has made considerable progress which greatly promotes the application of large-scale electrical energy storage in our daily life.<sup>1-6</sup> Lithium-sulfur (Li-S) batteries, because of their high theoretical specific capacity of 1675 mA h g<sup>-1</sup> and high theoretical specific energy of 2600 Wh kg<sup>-1</sup>, have received a great deal of attention.<sup>7-11</sup> Their practical energy density is expected to be 500–600 W h kg<sup>-1</sup>, which is around twice that of traditional lithium-ion batteries. Moreover, Li-S batteries show an inherently low competitive cost because of the abundance of sulfur.

Despite these promising features, practical applications of Li-S batteries are hindered by several obstacles.<sup>12-15</sup> One of the major issues is the short cycle life stemming from the dissolution of lithium polysulfides (LiPSs) into the liquid electrolytes and the migration of LiPSs between the anode and the cathode, which causes the so-called “shuttle effect” and would induce low discharge energy capacity and low Coulombic

efficiency. Besides, the relatively poor electrical conductivity of sulfur and the ~80% volume expansion during the cycling of sulfur will lead to low utilization of active materials and rapid aging of electrodes. Last but not least, the large energy barriers of the sulfur reduction reaction (SRR) during discharge and Li<sub>2</sub>S decomposition during charge lead to slow kinetics in Li-S batteries, greatly affect their performance.<sup>16, 17</sup> Therefore, the rational design of Li-S host materials should take into consideration not only the suppression of LiPSs shuttling, but also the catalytic activity of SRR and Li<sub>2</sub>S decomposition, the latter being long overlooked.

Two-dimensional (2D) materials have been demonstrated to be effective sulfur hosts with improved electrochemical performance for Li-S batteries.<sup>18-20</sup> Among them, 2D transition metal carbides and nitrides, named MXenes, have attracted much attention due to their excellent electronic conductivity, high surface area, controllable hierarchical structure, and physical confinement for electrode volume changes.<sup>21-26</sup> For instance, Liang *et al.* demonstrated that 70 wt% S/Ti<sub>2</sub>C composites exhibited long-term stability as cathodes and showed excellent cycling performance with a specific capacity close to 1200 mA h g<sup>-1</sup> at C/5 current rate;<sup>27</sup> Zhang *et al.* used a phase engineering strategy to fabricate Ti<sub>3</sub>C<sub>2</sub> MXene/1T-2H MoS<sub>2</sub>-C nanohybrids which greatly improved the capacity (1194.7 mAh g<sup>-1</sup> at 0.1 C), rate ability (677.2 mAh g<sup>-1</sup> at 2 C), and cycling stability (0.07% per cycle) in Li-S batteries.<sup>28</sup>

<sup>a</sup> Department of Applied Physics and Research Institute for Smart Energy, The Hong Kong Polytechnic University, Hung Hom, Kowloon, Hong Kong, P.R. China. E-mail: aphhuang@polyu.edu.hk

<sup>b</sup> State Key Laboratory of Optoelectronic Materials and Technologies, Centre for Physical Mechanics and Biophysics, School of Physics, Sun Yat-sen University, Guangzhou, Guangdong Province, P.R. China. E-Mail: luox77@mail.sysu.edu.cn

† Footnotes relating to the title and/or authors should appear here.

Electronic Supplementary Information (ESI) available: [details of any supplementary information available should be included here]. See DOI: 10.1039/x0xx00000x

Nevertheless, their bifunctional catalytic activities toward SRR and Li<sub>2</sub>S decomposition have not been investigated yet, and until now, the majority of studies about MXenes applied in Li-S batteries are focused on the carbides; more than 20 types of carbide MXenes having been synthesized while only a few nitride MXenes with higher conductivity than corresponding carbides are reported.<sup>21, 29, 30</sup> Recently, the successful synthesis of 2D V<sub>2</sub>N and Mo<sub>2</sub>N further expands the family of experimentally achievable 2D transition-metal nitrides.<sup>29</sup> Particularly, V<sub>2</sub>N MXene is worthy of attention because VN/graphene composite has been experimentally proven to have a number of desirable properties as a Li-S host material in a pioneer report.<sup>31</sup> For vanadium element, its multiple-valence-state feature (from V<sup>2+</sup> to V<sup>5+</sup>), stable crystalline framework when forming compounds, and rich distribution in the Earth's crust<sup>32</sup> endow V<sub>2</sub>N MXenes with great potential as sulfur hosts.

Except for the surface terminations (-O, -F, and -OH) which is commonly introduced during the MXenes synthesis process,<sup>33-35</sup> non-native functional groups, such as -S, also inevitably exist on the surface of MXenes when it is used in Li-S batteries. It is also reported that S-functionalized MXenes may exhibit lower Li<sub>2</sub>S decomposition barrier because of the trapping effect between Li atoms and S-containing surface.<sup>16</sup> Thus, the understanding of these surface groups, including the distribution and arrangement of surface terminations, is important in both theoretical studies and the interpretation of the resultant properties. In this work, we select V<sub>2</sub>N monolayer as a typical nitride MXene to systematically investigate its potential as a host material by means of DFT calculations. The electronic properties, anchoring strength, catalytic ability, and vacancy effect are comprehensively studied. Our calculations reveal that the anchoring strength and bifunctional catalytic ability of V<sub>2</sub>N can be modulated by the surface terminating groups (T=O, F, and S). The computational scheme in this work can open up a new avenue for the rational design of other 2D materials as hosts for S cathodes.

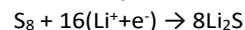
## 2. Computational methods

First-principles calculations were performed in the framework of DFT by the Vienna *ab initio* simulation package (VASP).<sup>36</sup> The exchange-correlation energy was described by the generalized gradient approximation (GGA) with the Perdew-Burke-Ernzerhof (PBE) flavor.<sup>37</sup> For geometry optimization, the plane-wave cut-off energy was set as 500 eV. The Brillouin-zone integration was performed using a Monkhorst-Pack grid of k-point sampling, and the meshes of  $\Gamma$ -centered 15×15×1 and 3×3×1 were used for the unit cell and the 4×4×1 supercell, respectively. During geometric relaxation, the convergence criteria for energy and force were set at 10<sup>-5</sup> eV and 0.01 eV Å<sup>-1</sup>, respectively, while for self-consistent field calculations, energy convergence criteria of 10<sup>-5</sup> eV was also used.

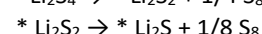
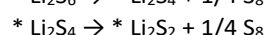
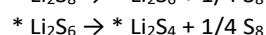
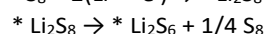
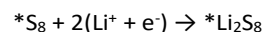
The van der Waals (vdW) interaction between V<sub>2</sub>N/V<sub>2</sub>NT<sub>2</sub> and Li<sub>2</sub>S<sub>n</sub> (S<sub>8</sub>) (n=1, 2, 4, 6, and 8) was considered by using the semiempirical DFT-D2<sup>38</sup> approach. A vacuum layer of 20 Å along the *c*-axis was added to the slabs to avoid the interlayer interaction. Furthermore, charge differential analysis was used

to estimate the charge redistribution and transfer. The climbing image nudged elastic band (CI-NEB) method<sup>39</sup> was applied to calculate the minimum diffusion energy barrier and decomposition barriers. To investigate the dynamical stability, the phonopy code was used to calculate the phonon dispersion spectra.<sup>40</sup> During all the calculations, all the atoms were fully relaxed.

In the discharge process of Li-S batteries, the overall reaction of the reduction of one S<sub>8</sub> molecule (SRR) to form eight Li<sub>2</sub>S molecules is a 16-electron process:<sup>17</sup>



and the elementary steps in the reaction pathway of generating one Li<sub>2</sub>S molecule is:<sup>41, 42</sup>



where \* denotes active sites on the catalyst surface. The Gibbs free energy change  $\Delta G$  of each step was calculated by:

$$\Delta G = \Delta E + \Delta ZPE - T\Delta S$$

where  $\Delta E$ ,  $\Delta ZPE$ , and  $T\Delta S$  represent the changes of DFT-calculated total energy, zero-point energy (ZPE), and entropic contribution, respectively. The ZPE and entropic contribution were calculated from the vibrational frequencies, and the temperature of 298 K was used.

## 3. Results and discussion

### 3.1 Structural and electronic properties of V<sub>2</sub>N and V<sub>2</sub>NT<sub>2</sub> monolayers

The V<sub>2</sub>N monolayer is built up of a sandwiched structure containing one N and two V layers in a sequence of V(1)-N-V(2) (Fig. 1a, b). The optimized V<sub>2</sub>N monolayer has the lattice parameters of  $a = b = 2.89$  Å and the thickness of  $c = 2.08$  Å. In the phonon dispersion spectra, the absence of imaginary phonon modes in the first Brillouin zone indicates that the V<sub>2</sub>N monolayer is dynamically stable (Fig. S1).<sup>40, 43</sup> For the V<sub>2</sub>NT<sub>2</sub> monolayers, the most favorable site for terminating groups T are determined by performing the total energy calculations. Three possible high-symmetry sites  $\alpha$ ,  $\beta$ , and  $\gamma$  are considered (Fig. 1b), and the total energies of all possible V<sub>2</sub>NT<sub>2</sub> phases are listed in Table S1. Based on the analysis,  $\alpha$  site is the most favorable adsorption site (Fig. 1c-f). With the terminal groups, both V(1)-N and V(2)-N bonds are elongated (Table S2), implying that the terminal atoms strongly interact with the original V<sub>2</sub>N monolayer. **The thermal stability of the V<sub>2</sub>NT<sub>2</sub> was verified by *ab initio* molecular dynamics (AIMD) simulations (Fig. S2).** Moreover, we also obtain the lowest energy configuration of the isolated S<sub>8</sub> and Li<sub>2</sub>S<sub>n</sub> molecules by DFT calculations, as shown in Fig. 1g and S3. The structural parameters and symmetries of our configurations are very close to those obtained by B3LYP/6-311G(3df)-level quantum chemistry calculations<sup>44</sup> and structure prediction using particle-swarm optimization algorithm<sup>45</sup> with negligible differences.

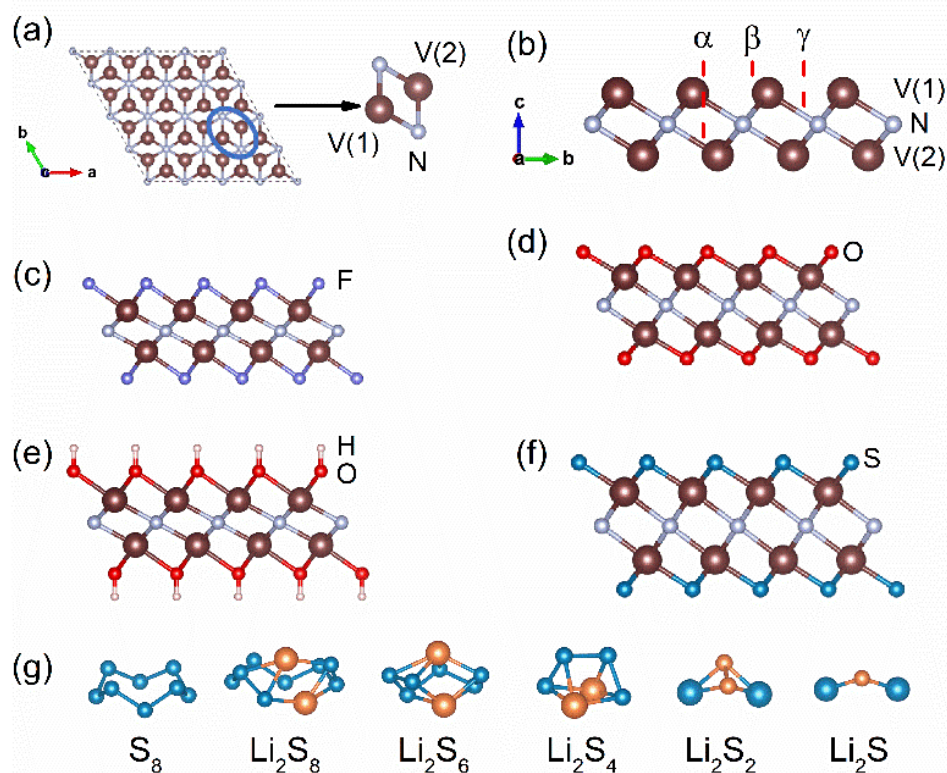


**Fig. 1** DFT-optimized structures. (a) Top views of  $V_2N$ ; (b) Side view of  $V_2N$ , (c)  $V_2NO_2$ , (d)  $V_2NF_2$ , (e)  $V_2N(OH)_2$ ; (f)  $V_2NS_2$ ; (g)  $S_8$  and  $Li_2S_n$  ( $n=1, 2, 4, 6$  and  $8$ ) structures. V, N, O, F, H, S and Li atoms are represented in brown, grey, red, purple, pink, blue and orange, respectively.

The metallicity of sulfur host material is an important factor to consider for Li-S battery application. Based on the calculated electronic density of states (DOS) of  $V_2N$  and  $V_2NT_2$ , both the bare and terminated ( $V_2N$  and  $V_2NT_2$ ) phases exhibit excellent metallicity and the majority of electron states at the Fermi level are originated from the V-4d orbitals (Fig. 2), with very little contribution from the non-metal atoms. As a result, the excellent metallic characters of  $V_2N$  and  $V_2NT_2$  are expected to improve the electrochemical performance of Li-S cells. Since sulfur and short-chain LiPSs ( $Li_2S_2$  and  $Li_2S$ ) exhibit insulating behavior,<sup>42</sup> the metallicity of  $V_2N$  and  $V_2NT_2$  is particularly significant for the electron transfer in the bifunctional catalytic reaction (SRR and  $Li_2S$  decomposition).

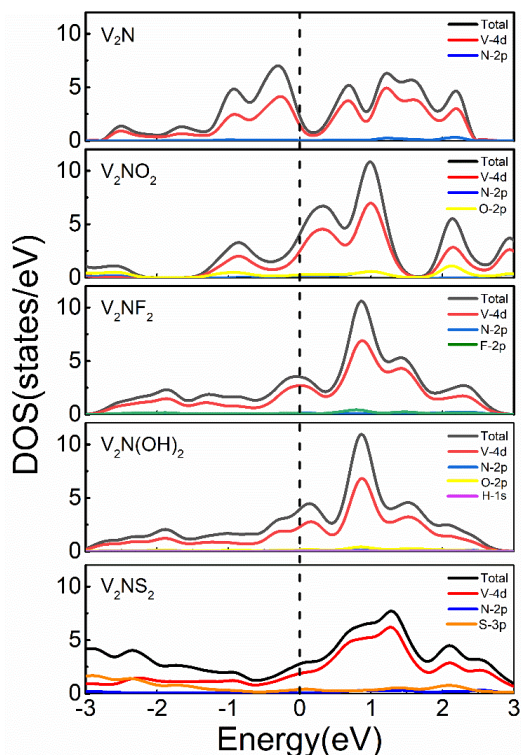


**Fig. 2** Total and partial density of states for 2D  $V_2N$  and  $V_2NT_2$  ( $T=O, F, OH,$  and  $S$ ). Fermi levels are set to be zero (denoted in black dotted line).

### 3.2 Anchoring ability for $S_8$ and $Li_2S_n$

The anchoring effect of  $V_2N$  and  $V_2NT_2$  monolayers is evaluated by calculating the adsorption energies. We have conducted a comprehensive search for the most energy favorable adsorption sites for each  $S_8$  and  $Li_2S_n$  species. To be specific, we have tested three symmetry unique sites ( $\alpha, \beta,$  and  $\gamma$ ) and two different rotational orientations on the host surface (Fig. S4, with a total number of 180 different structures) for each compound to obtain the most stable adsorption site and configuration. The results showed that the adsorption strength of  $S_8$  and  $Li_2S_n$  on bare  $V_2N$  is extremely strong, as indicated by the large adsorption energy values in the range from -5 to -25 eV (Fig. 3a). However, with such a large adsorption strength, the  $S_8$  and  $Li_2S_n$  are easily decomposed into single S (and Li) atoms, which are then tightly captured by the outer V layer of  $V_2N$  monolayers (Fig. 3b, c, and d). Thus, bare  $V_2N$  is not suitable for direct application in Li-S batteries, and it will automatically transform to S-functionalized  $V_2N$  upon  $S_8$  adsorption, so it is not discussed in the following sections.

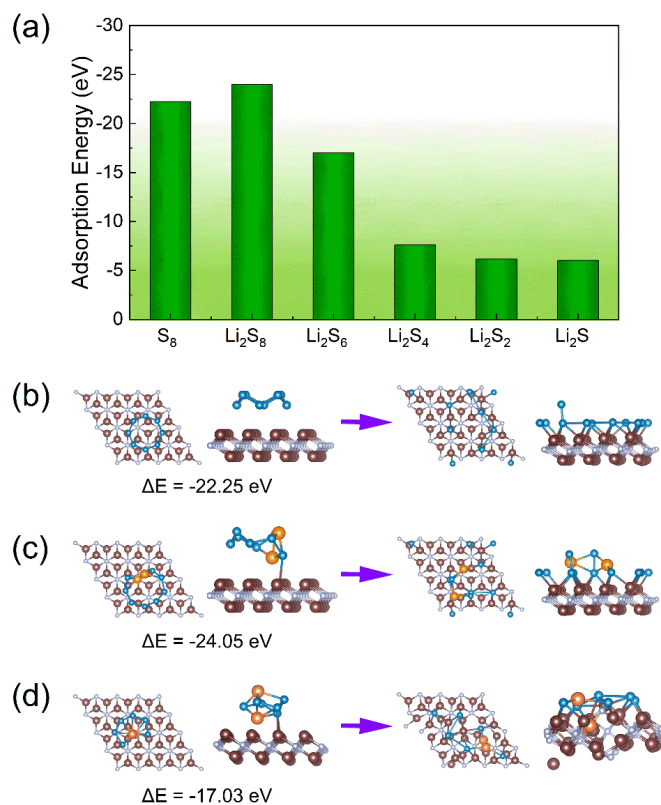


**Fig. 3** (a) Adsorption energies of  $S_8$  and  $Li_2S_n$  on  $V_2N$ ; adsorption structures of (b)  $S_8$ , (c)  $Li_2S_8$ , and (d)  $Li_2S_6$  on  $V_2N$  before (left) and after (right) optimization. The V, N, Li, and S atoms are distinguished by brown, gray, orange, and blue color, respectively.

For all the functionalized  $V_2NT_2$  structures, the adsorption strengths of  $S_8$  and  $Li_2S_n$  on  $V_2N(OH)_2$  are relatively stronger than  $V_2NO_2$ ,  $V_2NF_2$ , and  $V_2NS_2$  during the whole lithiation process (Fig. 4a). However,  $V_2N(OH)_2$  become unstable after adsorption of  $Li_2S_n$  species, where H atoms spontaneously migrate toward S atoms in the  $Li_2S_n$  while the remaining O atoms interact with Li atoms, leading to the breakage of the  $Li_2S_n$  species eventually (Fig. 4d). For  $V_2NO_2$ ,  $V_2NF_2$ , and  $V_2NS_2$  monolayers, on the contrary, the structures remain stable, which indicates the relatively mild adsorption strength (Fig. 4b, c, and e). We also identify the interactions between  $V_2NT_2$  and  $S_8/Li_2S_n$  by comparing the adsorption energies with and without vdW corrections. From the ratio of vdW ( $R_{vdW} = \frac{E_{ads}^{vdW} - E_{ads}^{no\ vdW}}{E_{ads}^{vdW}} \times 100\%$ ) results (Fig. S5), we can conclude that physical interactions (vdW) play a major role in the adsorption of  $S_8/Li_2S_n$  on  $V_2NS_2$ , exhibiting  $R_{vdW}$  values higher than 90%. For  $V_2NF_2$  and  $V_2NO_2$ , on the other hand, with relatively lower  $R_{vdW}$  values especially for  $S_8$  and long-chain LiPSs, implies that chemical interactions also contribute a lot to the  $S_8/Li_2S_n$  adsorption. In short, the vdW interaction should be considered when studying the adsorption form of LiPSs on  $V_2NT_2$  monolayers.

In addition, since there are usually small amounts of vacancies on the surface of MXenes, we also investigate the vacancy effect based on the structure of  $V_2NO_{2-x}/V_2NF_{2-x}/V_2NS_{2-x}$  ( $x = 1/16$ ). Similar to the intact  $V_2NO_2/V_2NF_2/V_2NS_2$ , none of the adsorbed  $Li_2S_n$  structures exhibit a tendency of decomposition, and the adsorption of  $Li_2S_n$

( $S_8$ ) on  $V_2NO_{2-x}/V_2NF_{2-x}/V_2NS_{2-x}$  ( $x = 1/16$ ) is energetically favorable (Fig. S6). This can be attributed to the electron-rich regions with lone-pair electrons induced by the O/F/S vacancy, as indicated by the electron localization functions (ELF) results (marked by red arrows in Fig. S7),<sup>46</sup> and after  $Li_2S_n$  ( $S_8$ ) species are adsorbed on the surface of  $V_2NT_{2-x}$ , they can form chemical bonds with the vacancy sites through those electrons, which

lead to the easy bonding with the S of  $Li_2S_n$  ( $S_8$ ). Consequently, for nitride-based MXenes, the shuttle suppression ability would not be hampered by the small amount of vacancies in Li-S batteries.

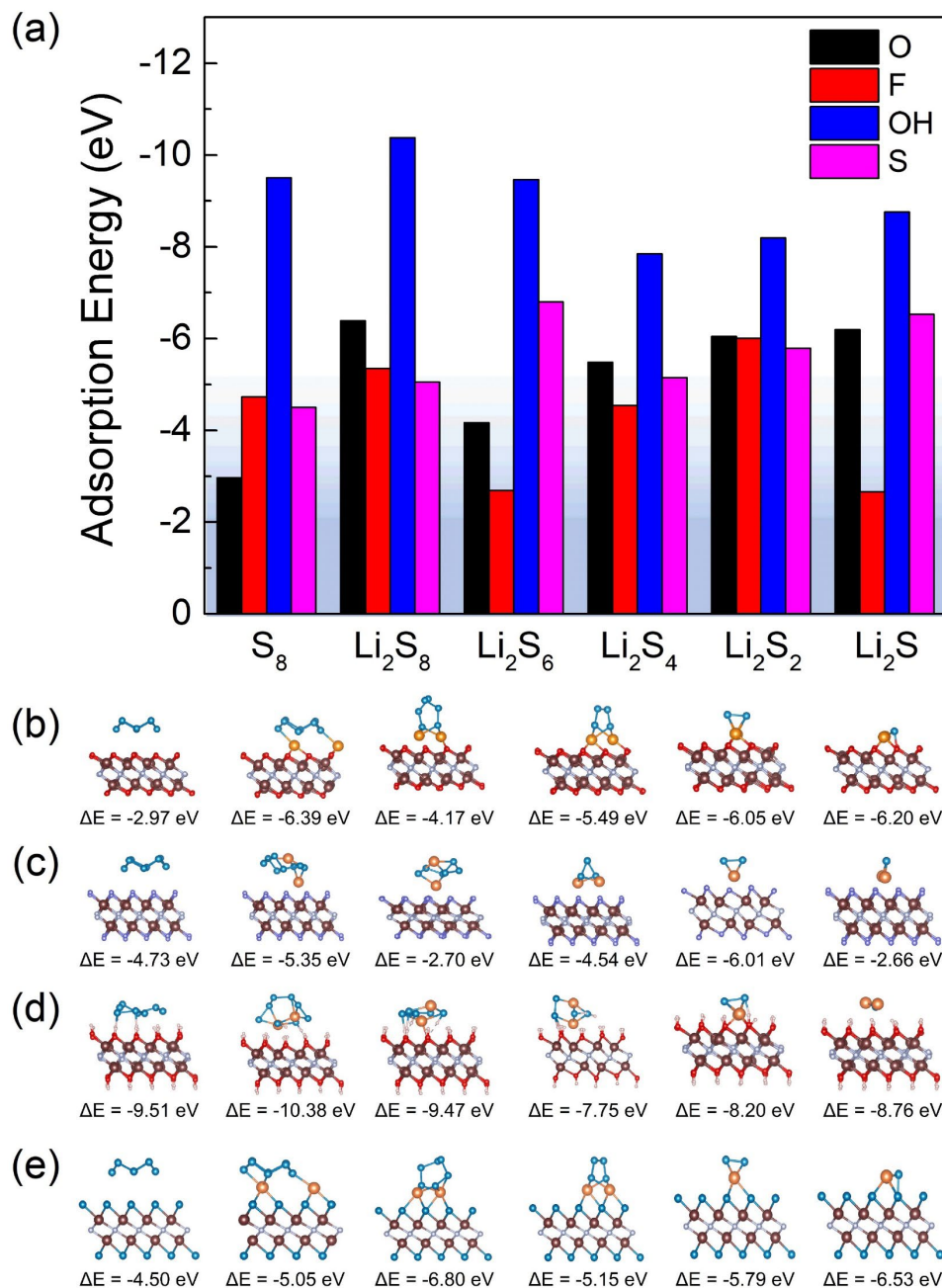


**Fig. 4** (a) Adsorption energies of  $S_8$  and  $Li_2S_n$  on  $V_2NT_2$  ( $T=O, F, OH,$  and  $S$ ), and the corresponding optimized structures of  $S_8$  and  $Li_2S_n$  on the surface of (b)  $V_2NO_2$ , (c)  $V_2NF_2$ , (d)  $V_2N(OH)_2$ , and (e)  $V_2NS_2$ . The adsorption energy values are marked under each structure. The V, N, O, F, H, Li, and S atoms are distinguished by brown, gray, red, purple, pink, orange, and blue color, respectively.

To verify the ability of surface terminations in suppressing the LiPS shuttling, it is necessary to evaluate the binding effects between polysulfides and 1,3-dioxolane (DOL) / 1,2-dimethoxyethane (DME) electrolyte.<sup>47, 48</sup> Through comparing

the two different types of adsorption energy ( $E_{V_2NT_2+S_8/Li_2S_n}$  and  $E_{DOL/DME+S_8/Li_2S_n}$ ), we found that the  $S_8$  and  $Li_2S_n$  prefer to be adsorbed on  $V_2NT_2$  rather than DOL/DME molecules since the adsorption energies between LiPSs and DOL/DME

molecules were between -1 and 0 eV (Fig. S8), larger than those between LiPSs and  $V_2NT_2$  monolayers (Fig. 4a). Based on the above discussion, the  $V_2NO_2$ ,  $V_2NF_2$ , and  $V_2NS_2$  can not only fix  $S_8$  and  $Li_2S_n$  on their surfaces but also maintain stably their own structures. Thus, they exhibit great potential in preventing polysulfide dissolution and shuttling in the electrolyte.

To assess the nature of the interaction between the host material and polysulfides, the charge density difference is also analyzed. Taking  $V_2NO_2$  as an example (Fig. 5a), for  $S_8$ , obvious charge transfer exhibits between S and V, indicating the formation of polar covalent bonds between V and S. For other  $Li_2S_n$  structures, electron accumulation regions (yellow) appear between the Li atoms and the outer O layer, while electron depletion (blue) happens around the Li-S and S-S bonds, explaining the binding behavior of  $Li_2S_n$  on  $V_2NO_2$  with the formation of Li-O bonds. Similar phenomenon can be observed in  $V_2NF_2$  and  $V_2NS_2$  (Fig. 5b, c).

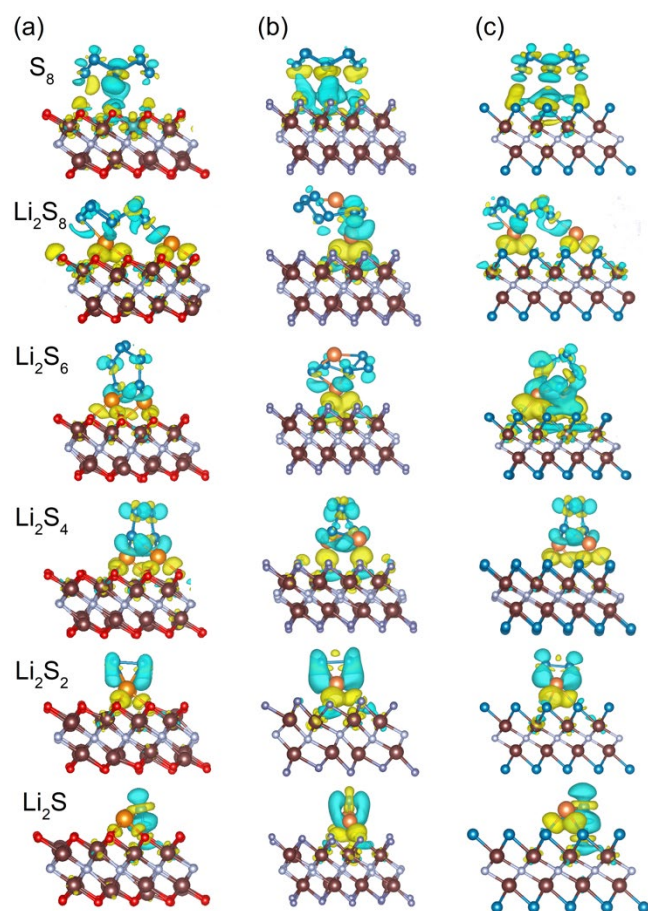


**Fig. 5** Charge density difference of  $S_8$  and  $Li_2S_n$  adsorbed on (a)  $V_2NO_2$ , (b)  $V_2NF_2$ , and (c)  $V_2NS_2$ . Yellow and blue regions indicate electron accumulation and depletion, respectively. The V, N, O, F, Li and S atoms are distinguished by brown, gray, red, purple, orange, and blue color, respectively.

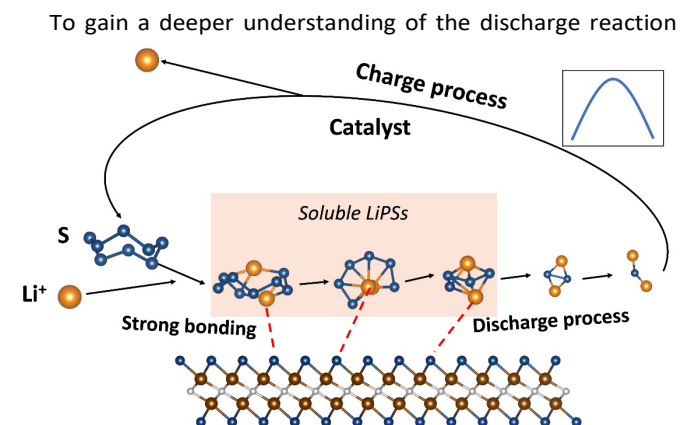
### 3.3 Bifunctional catalytic performance and $Li^+$ diffusion kinetics for Li-S batteries

Aside from the anchoring ability, the diffusion properties and catalytic effect are also key indicators for Li-S batteries. In the discharge process, the fast kinetics of  $S_8$  reduction to long-chain soluble LiPSs ( $Li_2S_8$ ,  $Li_2S_6$ , and  $Li_2S_4$ ), and finally short-chain insoluble LiPSs ( $Li_2S_2$  and  $Li_2S$ ) could shorten the LiPS accumulation time in the cathode and thus reduce the LiPS dissolution. The final discharge product,  $Li_2S$ , which suffers from low  $Li^+$  diffusivity and high decomposition energy barrier greatly affects the conversion between the polysulfides and will cause high overpotential and low-rate capability. Thus, the decomposition kinetics of LiPSs during discharge and that of  $Li_2S$  during charge processes, as well as  $Li^+$  diffusion on hosts, are all vital for the kinetic performance of Li-S batteries.

To analyze the decomposition kinetics of  $Li_2S$  on  $V_2NT_2$ , the CI-NEB method is used. The decomposition process can be described by the following equation:  $Li_2S \rightarrow LiS + Li^+ + e^-$ . That is, a  $Li_2S$  molecule can be decomposed into a LiS cluster by releasing a single Li atom, which corresponds to a charging process. The natural decomposition barrier of  $Li_2S$  is calculated to be 3.64 eV, while the decomposition barriers on  $V_2NO_2$ ,  $V_2NF_2$ , and  $V_2NS_2$  are remarkably reduced to 1.55, 2.31, and 1.19 eV (Fig. S9), respectively. Thus, surface functionalization can efficiently catalyze the  $Li_2S$  decomposition and reduce the overpotential of Li-S batteries, especially for  $V_2NO_2$  and  $V_2NS_2$  (Table 1). Besides, the diffusion barriers were studied to discuss the  $Li^+$  diffusion on host materials. The energy profiles along the  $Li^+$  diffusion coordinate show much smaller barriers than decomposition, the minimum  $Li^+$  diffusion barriers on  $V_2NO_2$ ,  $V_2NF_2$ , and  $V_2NS_2$  were 0.21, 0.17, and 0.16 eV, respectively (Fig. S10). These values are comparable to or smaller than those for other MXenes such as  $V_2CO_2$  (0.26 eV),  $Ti_3CNO_2$  (0.26 eV), and  $Ti_2NS_2$  (0.17 eV) (Table S3).<sup>45, 49-51</sup> The low  $Li_2S$  decomposition and  $Li^+$  diffusion barriers imply the improved kinetics during  $Li_2S$  decomposition and  $Li^+$  diffusion, which can accelerate the whole charging process in the Li-S batteries.

**Table 1.** Calculated  $Li_2S$  decomposition barriers,  $Li^+$  diffusion barriers, and  $\Delta G$  of rate-limiting step during the SRR on  $V_2NO_2$ ,  $V_2NF_2$ , and  $V_2NS_2$ .

Substrate	$Li_2S$ Decomposition barrier (eV)	$Li^+$ diffusion barrier (eV)	$\Delta G$ of rate-limiting step during the SRR (eV)
$V_2NO_2$	1.55	0.21	1.88
$V_2NF_2$	2.31	0.17	2.14
$V_2NS_2$	1.19	0.16	0.49



kinetics of polysulfides on the hosts (i.e. SRR), the overall reactions based on the reversible formation of  $\text{Li}_2\text{S}$  from  $\text{S}_8$  and Li bulk were considered (Fig. 6). The Gibbs free energies for all the reaction steps in SRR are calculated and the evolution profiles (from  $\text{S}_8$  to  $\text{Li}_2\text{S}$  species) for  $\text{V}_2\text{NO}_2$ ,  $\text{V}_2\text{NF}_2$ , and  $\text{V}_2\text{NS}_2$  are exhibited.

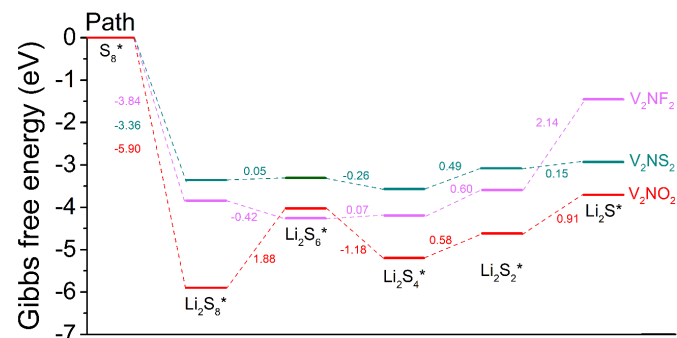


**Fig. 6** Gibbs free energy profiles for the sulfur reduction reaction on  $\text{V}_2\text{NO}_2$ ,  $\text{V}_2\text{NF}_2$ , and  $\text{V}_2\text{NS}_2$ .

For  $\text{V}_2\text{NO}_2$ , it can be seen that the reduction steps from  $\text{S}_8$  to the  $\text{Li}_2\text{S}_8$  and from  $\text{Li}_2\text{S}_6$  to the  $\text{Li}_2\text{S}_4$  are exothermic, with the Gibbs free energy change ( $\Delta G$ ) values of  $-5.90$  and  $-1.18$  eV, respectively. The other three reduction steps, from  $\text{Li}_2\text{S}_8$  to  $\text{Li}_2\text{S}_6$ ,  $\text{Li}_2\text{S}_4$  to  $\text{Li}_2\text{S}_2$ , and  $\text{Li}_2\text{S}_2$  to  $\text{Li}_2\text{S}$ , are all endothermic, and among them, the step from  $\text{Li}_2\text{S}_8$  to  $\text{Li}_2\text{S}_6$  exhibit the largest  $\Delta G$  value of  $1.88$  eV, which is determined as the rate-limiting step (RLS). For  $\text{V}_2\text{NF}_2$ , two exothermic reaction steps include those from  $\text{S}_8$  to  $\text{Li}_2\text{S}_8$  and from  $\text{Li}_2\text{S}_8$  to  $\text{Li}_2\text{S}_6$ , while the other three steps are endothermic steps, and RLS is the last step ( $\text{Li}_2\text{S}_2$  to  $\text{Li}_2\text{S}$ ) with  $\Delta G$  of  $2.14$  eV. The significant differences in  $\Delta G$  of step  $\text{Li}_2\text{S}_8 \rightarrow \text{Li}_2\text{S}_6$  and step  $\text{Li}_2\text{S}_2 \rightarrow \text{Li}_2\text{S}$  for the three systems are related to the differences in their anchoring abilities of LiPSs: for  $\text{V}_2\text{NO}_2$ , the  $\text{Li}_2\text{S}_8$  adsorption is the strongest among the three systems, and its  $\text{Li}_2\text{S}_6$  anchoring ability is relatively weak (Fig. 4), leading to its high  $\text{Li}_2\text{S}_8 \rightarrow \text{Li}_2\text{S}_6$  barrier; for  $\text{V}_2\text{NF}_2$ , the adsorption strength of  $\text{Li}_2\text{S}$  is significantly decreased compared with that of  $\text{Li}_2\text{S}_2$ , while for  $\text{V}_2\text{NO}_2$  and  $\text{V}_2\text{NS}_2$ , the  $\text{Li}_2\text{S}_2$  and  $\text{Li}_2\text{S}$  adsorption energies are relatively close to each other (Fig. 4). Among all three structures,  $\text{V}_2\text{NS}_2$  exhibits the smallest  $\Delta G$  value for RLS in SRR ( $0.49$  eV,  $\text{Li}_2\text{S}_4$  to  $\text{Li}_2\text{S}_2$ , see Table 1) due to moderate LiPSs

adsorption. Thus, its outstanding bifunctional catalytic activity during charge ( $\text{Li}_2\text{S}$  decomposition) and discharge (SRR) can be achieved simultaneously. In combination with its metallic behavior and moderate anchoring ability of LiPSs,  $\text{V}_2\text{NS}_2$  can be an outstanding host material for Li-S batteries (Fig. 7).

**Fig. 7** Schematics of 2D  $\text{V}_2\text{NS}_2$  MXenes as promising sulfur hosts for Li-S battery applications.

## 4. Conclusions

In summary, we have explored the potential applications of 2D  $\text{V}_2\text{N}/\text{V}_2\text{NT}_2$  monolayers as the S cathode host for Li-S batteries by means of DFT calculations. It was shown that both bare and functionalized  $\text{V}_2\text{NT}_2$  monolayers exhibited excellent metallic character. However, bare  $\text{V}_2\text{N}$  cannot be directly used in Li-S batteries because of the extremely strong V-S or V-Li bond. Among the four functional groups (O/F/OH/S) studied,  $\text{V}_2\text{NS}_2$  monolayer is identified as the most promising candidate through a comprehensive examination on its metallicity, LiPS anchoring ability,  $\text{Li}_2\text{S}$  decomposition barrier,  $\text{Li}^+$  diffusion barrier, and SRR thermodynamics. This study gives insightful guidance to further experimental work on nitride MXenes and other novel 2D materials as promising host materials for Li-S batteries.

## Author contributions

**Ke Fan:** Conceptualization, Data curation, Investigation, Software, Methodology, Writing – original draft; **Yiran Ying:** Data curation, Writing – review & editing; **Xin Luo:** Supervision, Writing – review & editing; **Haitao Huang:** Funding acquisition, Supervision, Writing – review & editing.

## Conflicts of interest

There are no conflicts to declare.

## Acknowledgements

This work was supported by the Research Grants Council of the Hong Kong Special Administrative Region, China (Project No. PolyU152178/20E), the Hong Kong Polytechnic University (Project No. RHA3), and Science and Technology Program of Guangdong Province of China (Project Nos. 2019A050510012 and 2020A0505090001). X. L. thanks support from NSFC (No. 11804286) and the Fundamental Research Funds for the Central Universities (No. 19lgpy263), and the resources of the National Supercomputer Center in Guangzhou supported by the Special

Program for Applied Research on Super Computation of the NSFC Guangdong Joint Fund (second phase).

## References

1. Y. Yang, S. Bremner, C. Menictas and M. Kay, *Renewable and Sustainable Energy Reviews*, 2018, **91**, 109-125.
2. H. Chen, T. N. Cong, W. Yang, C. Tan, Y. Li and Y. Ding, *Progress in Natural Science*, 2009, **19**, 291-312.
3. D. G. Ladha, *Materials Today Chemistry*, 2019, **11**, 94-111.
4. Z. Rao and S. Wang, *Renewable and Sustainable Energy Reviews*, 2011, **15**, 4554-4571.
5. Q. He, B. Yu, Z. Li and Y. Zhao, *Energy & Environmental Materials*, 2019, **2**, 264-279.
6. X. Li, K. Li, S. Zhu, K. Fan, L. Lyu, H. Yao, Y. Li, J. Hu, H. Huang and Y. W. Mai, *Angewandte Chemie International Edition*, 2019, **58**, 6239-6243.
7. M. Barghamadi, A. Kapoor and C. Wen, *Journal of The Electrochemical Society*, 2013, **160**, A1256-A1263.
8. X. Ji and L. F. Nazar, *Journal of Materials Chemistry*, 2010, **20**, 9821-9826.
9. A. Fotouhi, D. J. Auger, L. O'Neill, T. Cleaver and S. Walus, *Energies*, 2017, **10**, 1937.
10. S. Walus, Université Grenoble Alpes, 2015.
11. X.-B. Cheng, J.-Q. Huang and Q. Zhang, *Journal of The Electrochemical Society*, 2017, **165**, A6058.
12. M. R. Busche, P. Adelhelm, H. Sommer, H. Schneider, K. Leitner and J. Janek, *Journal of Power Sources*, 2014, **259**, 289-299.
13. D. Liu, C. Zhang, G. Zhou, W. Lv, G. Ling, L. Zhi and Q. H. Yang, *Advanced science*, 2018, **5**, 1700270.
14. G. Gao, F. Zheng, F. Pan and L.-W. Wang, *Advanced Energy Materials*, 2018, **8**, 1801823.
15. L. Fan, M. Li, X. Li, W. Xiao, Z. Chen and J. Lu, *Joule*, 2019, **3**, 361-386.
16. G. Zhou, H. Tian, Y. Jin, X. Tao, B. Liu, R. Zhang, Z. W. Seh, D. Zhuo, Y. Liu and J. Sun, *Proc. Natl. Acad. Sci. U. S. A.*, 2017, **114**, 840-845.
17. L. Peng, Z. Wei, C. Wan, J. Li, Z. Chen, D. Zhu, D. Baumann, H. Liu, C. S. Allen and X. Xu, *Nat. Catal.*, 2020, **3**, 762-770.
18. M. Jana, R. Xu, X.-B. Cheng, J. S. Yeon, J. M. Park, J.-Q. Huang, Q. Zhang and H. S. Park, *Energy & Environmental Science*, 2020, **13**, 1049-1075.
19. L. Zhou, D. L. Danilov, R. A. Eichel and P. H. L. Notten, *Advanced Energy Materials*, 2020, DOI: 10.1002/aenm.202001304, 2001304.
20. X. Chen, H.-J. Peng, R. Zhang, T.-Z. Hou, J.-Q. Huang, B. Li and Q. Zhang, *ACS Energy Letters*, 2017, **2**, 795-801.
21. B. Anasori, Y. Xie, M. Beidaghi, J. Lu, B. C. Hosler, L. Hultman, P. R. C. Kent, Y. Gogotsi and M. W. Barsoum, *ACS Nano*, 2015, **9**, 9507-9516.
22. B. Anasori, M. R. Lukatskaya and Y. Gogotsi, *Nature Reviews Materials*, 2017, **2**, 16098.
23. Z. Xiao, Z. Li, X. Meng and R. Wang, *Journal of Materials Chemistry A*, 2019, **7**, 22730-22743.
24. C. Zhang, L. Cui, S. Abdolhosseinzadeh and J. Heier, *InfoMat*, 2020, **2**, 613-638.
25. K. Fan, Y. Ying, X. Li, X. Luo and H. Huang, *J. Phys. Chem. C*, 2019, **123**, 18207-18214.
26. X. Xu, Y. Zhang, H. Sun, J. Zhou, F. Yang, H. Li, H. Chen, Y. Chen, Z. Liu and Z. Qiu, *Adv. Electron. Mater.*, 2021, **7**, 2000967.
27. X. Liang, A. Garsuch and L. F. Nazar, *Angew Chem Int Ed Engl*, 2015, **54**, 3907-3911.
28. Y. Zhang, Z. Mu, C. Yang, Z. Xu, S. Zhang, X. Zhang, Y. Li, J. Lai, Z. Sun and Y. Yang, *Adv. Funct. Mater.*, 2018, **28**, 1707578.
29. P. Urbankowski, B. Anasori, K. Hantanasirisakul, L. Yang, L. Zhang, B. Haines, S. J. May, S. J. L. Billinge and Y. Gogotsi, *Nanoscale*, 2017, **9**, 17722-17730.
30. X. Xiao, H. Yu, H. Jin, M. Wu, Y. Fang, J. Sun, Z. Hu, T. Li, J. Wu and L. Huang, *ACS Nano*, 2017, **11**, 2180-2186.
31. Z. Sun, J. Zhang, L. Yin, G. Hu, R. Fang, H. M. Cheng and F. Li, *Nat Commun*, 2017, **8**, 14627.
32. M. Chen, Q. Liu, Z. Hu, Y. Zhang, G. Xing, Y. Tang and S. L. Chou, *Adv. Energy Mater.*, 2020, **10**, 2002244.
33. S. Lai, J. Jeon, S. K. Jang, J. Xu, Y. J. Choi, J.-H. Park, E. Hwang and S. Lee, *Nanoscale*, 2015, **7**, 19390-19396.
34. M. Naguib, R. R. Unocic, B. L. Armstrong and J. Nanda, *Dalton transactions*, 2015, **44**, 9353-9358.
35. M. Naguib, O. Mashtalir, J. Carle, V. Presser, J. Lu, L. Hultman, Y. Gogotsi and M. W. Barsoum, *ACS nano*, 2012, **6**, 1322-1331.
36. G. Kresse and J. Furthmüller, *Phys. Rev. B*, 1996, **54**, 11169.
37. J. P. Perdew, K. Burke and M. Ernzerhof, *Phys. Rev. Lett.*, 1996, **77**, 3865.
38. S. Grimme, *J. Comput. Chem.*, 2006, **27**, 1787-1799.
39. G. Henkelman, B. P. Uberuaga and H. Jónsson, *J. Chem. Phys.*, 2000, **113**, 9901-9904.
40. A. Togo and I. Tanaka, *Scr. Mater.*, 2015, **108**, 1-5.
41. R. S. Assary, L. A. Curtiss and J. S. Moore, *J. Phys. Chem. C*, 2014, **118**, 11545-11558.
42. X. Song, Y. Qu, L. Zhao and M. Zhao, *ACS Appl. Mater. Interfaces*, 2021, **13**, 11845-11851.
43. K. Fan, Y. Ying, X. Luo and H. Huang, *Physical Chemistry Chemical Physics*, 2020, **22**, 16665-16671.
44. L. Wang, T. Zhang, S. Yang, F. Cheng, J. Liang and J. Chen, *J. Energy Chem.*, 2013, **22**, 72-77.
45. D. Wang, F. Li, R. Lian, J. Xu, D. Kan, Y. Liu, G. Chen, Y. Gogotsi and Y. Wei, *ACS Nano*, 2019, **13**, 11078-11086.
46. S. Zhang, Q. Wang, Y. Kawazoe and P. Jena, *Journal of the American Chemical Society*, 2013, **135**, 18216-18221.
47. S. S. Zhang, *Journal of Power Sources*, 2013, **231**, 153-162.
48. J. Scheers, S. Fantini and P. Johansson, *Journal of Power Sources*, 2014, **255**, 204-218.
49. Y. Wang, J. Shen, L.-C. Xu, Z. Yang, R. Li, R. Liu and X. Li, *Phys. Chem. Chem. Phys.*, 2019, **21**, 18559-18568.
50. V. Shukla, N. K. Jena, S. R. Naqvi, W. Luo and R. Ahuja, *Nano Energy*, 2019, **58**, 877-885.
51. X. Chen, Z. Kong, N. Li, X. Zhao and C. Sun, *Physical Chemistry Chemical Physics*, 2016, **18**, 32937-32943.